

A Study on Microstructural Parameters for the Characterization of Granular Porous Ceramics Using a Combination of Stochastic and Mechanical Modeling

MATTHIAS KULOSA*

MATTHIAS NEUMANN†

MARTIN BOEFF*

GERD GAISELMANN†

VOLKER SCHMIDT†

ALEXANDER HARTMAIER*

* *Ruhr-Universität Bochum, Interdisciplinary Centre for Advanced Materials Simulation (ICAMS), Universitätsstr. 150, 44801, Bochum, Germany*

† *Universität Ulm, Institut für Stochastik, 89069 Ulm, Germany*

To correlate the mechanical properties of granularporous materials with their microstructure, typically porosity is being considered as the dominant parameter. In this work, we suggest the average coordination number, i.e. the average number of connections that each grain of the porous material has to its neighboring grains, as additional - and possibly even more fundamental - microstructural parameter. In this work, a combination of stochastic and mechanical modeling is applied to study microstructural influences on the elastic properties of porous ceramics. This is accomplished by generating quasi two-dimensional (2D) and fully three-dimensional (3D) representative volume elements (RVE) with tailored microstructural features by a parametric stochastic microstructure model. In the next step, the elastic properties of the RVEs are characterized by finite element analysis. The results reveal that the average coordination number exhibits a very strong correlation with the Young's modulus of the material in both, 2D and 3D RVEs. Moreover, it is seen that quasi-2D RVEs with the same average coordination number, but largely different porosities, only differ very slightly in their elastic properties such that the correlation is almost unique. This finding is substantiated and discussed in terms of the load distribution in microstructures with different porosities and average coordination numbers.

Keywords: Microstructure-property relation; Stochastic modeling; Porous ceramic.

1. Introduction

Ceramic materials, like alumina or zirconia, exhibit interesting properties such as thermal and chemical resistance, high hardness, low electrical conductivity and good wear resistance. Because of these positive aspects ceramic materials are of interest for different technical applications e.g. vehicle disc brakes, coatings of turbine blades, filters, membranes, insulators or biomedical implants. In particular, applications like

filters and heat insulators require a certain porosity of the material. However, small defects like pores dramatically decrease the strength of the material due to the brittleness of ceramics. Nevertheless, porous ceramics are used as matrix materials in fiber-reinforced ceramic composites (Göring et al., 2007; Schmücker et al., 2003) and are analyzed both in experiments (Nanjangud et al., 1995; Zok and Levi, 2001; Mattoni et al., 2001) and in computational materials science (Sadowski and Samborski, 2003; Smolin et al., 2014). For example it has been found by Sadowski and Samborski (2003) that the Young's modulus also depends on whether or not pores are interacting.

Especially in experimental work, porosity is typically considered as the main parameter of interest. The results of several studies showed that porosity directly affects the mechanical properties. In Nanjangud et al. (1995) a correlation between the green densities of different specimens and the Young's modulus of ceramics was found, whereas in Zok and Levi (2001) and in Mattoni et al. (2001) the focus was put on the relationship between porosity of the matrix phase and macroscopic behavior of ceramic based composites. These investigations showed that elastic constants, as the Young's modulus, correlate with porosity. While a linear relationship between porosity and Young's modulus for porosities from 0 % to 25 % was found in Asmani et al. (2001) and Gatt et al. (2005), a quadratic relationship for porosities greater than 55% was found with a decreasing slope towards high porosities, see Magdeski (2010). Moreover, the relationship between porosity, mechanical properties and fracture toughness of ceramics is an ongoing discussion in the literature (Rice, 1984; Wiederhorn, 1984; Wagh et al., 1993; Jauffres et al., 2011).

All experimental studies mentioned above investigate the relationship between porosity and the mechanical properties of ceramics and ceramic composites, respectively. However, by Roberts and Garboczi (2000) it was pointed out that mechanical properties of ceramics depend not only on porosity, but also on pore shape of the microstructure. Different scenarios of virtual pore microstructures varying porosity and pore shape were simulated, more precisely, pores consisted of solid spheres, overlapping spherical particles or overlapping ellipsoids. For these virtual microstructures, the Poisson ratio and Young's modulus were computed by means of the finite element method (FEM). The results obtained by Roberts and Garboczi (2000) show that for a fixed porosity, variation of pore shape leads to different values of the computed mechanical properties. Further simulation work has also been conducted for foams, where for example the influence of structural disorder (Roschning and Huber, 2016) or the scaling with ligament size (Diebels and Steeb, 2002) has been studied.

This result gives rise to the assumption that there are further microstructural parameters than porosity, which are relevant for the mechanical properties of ceramics. In the present paper, a parametric stochastic microstructure model (PSMM) is used for generating representative volume elements (RVEs) of virtual granular porous microstructures. When generating the RVEs, the idea is that assemblies of

overlapping spherical grains provide a good geometric representation of a wide class of sintered ceramics. Porosity as well as average coordination number of sintered grains can be systematically varied by parameters of the stochastic model. The quasi-2D microstructures considered in this work are clearly not representative of real materials. However, we found that the possibility they offer to study larger systems makes them quite attractive such that it is of some interest to study the differences between 2D and 3D structures. In fact, our results reveal that some of the properties of quasi-2D microstructures are comparable to realistic 3D structures, while others are not, as will be discussed in detail later. In a further step, FEM is used to simulate mechanical loading of the structures. Using homogenization techniques, the stiffness tensor and hence the homogenized Young's modulus are calculated. This makes it possible to analyze the influence of microstructural parameters on mechanical properties of sintered porous ceramics.

It is noted here, that the term RVE is used in the sense that the considered volume elements are representative for all microstructures generated with the same parameters. We verified that using larger volumes does not reduce the scatter in the calculated properties significantly. Hence, the considered RVEs are large enough to represent a given set of microstructural parameters. However, we do not claim that the considered RVEs represent the properties of a specific material.

The present paper is organized as follows. In Section 2, the PSMM and the simulation of mechanical loading by FEM are described. In Section 3, the results of the performed simulations are presented and the relationship between microstructural parameters and mechanical properties is discussed. Finally, Section 4 concludes the paper.

2. Methods

In this section the method to generate representative volume elements describing the microstructures of porous sinter ceramics is described. Subsequently, the meshing of the RVEs is explained which enables the study of the mechanical response of different microstructures with FEM. Periodic boundary conditions are applied to the RVE and homogenization of the results yields effective elastic properties of the different microstructures.

Since the microstructure of porous ceramics is considered here as a network of overlapping spherical grains, the connectivity in this network is quantified by the average coordination number of the grains. Throughout the present paper, the coordination number N_C of an individual grain is defined as the number of neighboring grains that exhibit an overlap with the grain under consideration (German, 2014). The average coordination number \tilde{N}_C is consequently defined as the average value of the coordination numbers of all grains in the RVE.

2.1. *Microstructure generation*

To generate RVEs with varying porosity and connectivity, a parametric stochastic microstructure model (PSMM) is developed based on ideas of stochastic geometry (Chiu et al., 2013). By the aid of the PSMM virtual 2D and 3D microstructures consisting of ceramic and pore phase are generated. The ceramic phase is modeled as a union of moderately overlapping spheres with equal radii. The midpoints of the spheres are arranged such that the resulting network of overlapping spheres is completely connected. Moreover, the model allows us to control porosity, the degree of pairwise overlapping of spheres, which is formally defined in Equation (1), and the average coordination number. In the following a brief description of the PSMM is given.

The main idea of the PSMM is to generate an initial sphere system at first and then to rearrange the midpoints of the initial sphere system iteratively. The rearrangement is organized such that the resulting sphere system is completely connected with probability 1 while a certain criterion of pairwise overlapping between spheres is minimized. The PSMM is defined within an observation window $[0, w]^d$, $w > 0$ and $d \geq 2$. For the application considered in the present paper, $d = 2$ and $d = 3$ are the relevant cases.

Sphere systems with constant radius $r = 0.04 \mu m$ are considered. The midpoints of the initial sphere system, denoted by $\{S_i\}_{i=1}^N$, are modeled by a homogeneous Poisson point process (Chiu et al., 2013) in the sampling window W with intensity $\lambda > 0$. This means that the random number of spheres N is Poisson distributed with parameter $\lambda \nu_d(W)$ and under the condition that the system consists of $N = n$ spheres, the locations of their midpoints S_1, \dots, S_n are distributed completely at random in W . Here $\nu_d(W) = w^d$ denotes the d -dimensional volume of W . The porosity of the resulting RVE can be controlled by λ . Note that the sphere system in W is defined with respect to periodic boundary conditions, see Figure 1. This means that if a sphere sticks out of W at one side, the part of the sphere sticking out of W is included on the opposite side of W , see the right-hand side of Figure 1.

For the rearrangement of sphere midpoints, a definition of the criterion of pairwise overlap CO_ρ is needed. Therefore, the degree of overlap $O_{i,j}$ between two spheres S_i and S_j is introduced by $O_{i,j} = 2 - \delta(S_i, S_j)/r$, where $\delta(\cdot, \cdot)$ denotes the distance in W with respect to periodic boundary conditions. For a model parameter $\rho \in [0, 1]$, the criterion of pairwise overlap is then defined by

$$CO_\rho = \sum_{i=1}^n \sum_{j=i+1}^n (O_{i,j} - \rho) \mathbb{1}\{\rho < O_{i,j}\} \quad (1)$$

which is the sum over all degrees of overlaps corresponding to point pairs with an degree of overlap greater than ρ . Here $\mathbb{1}\{\cdot\}$ denotes the indicator function.

The initial sphere system is rearranged in order to obtain a completely connected sphere system, in which $O_{i,j}$ is close to ρ for each pair of overlapping spheres S_i and S_j . During the iterative rearrangement of the sphere system, repulsion and

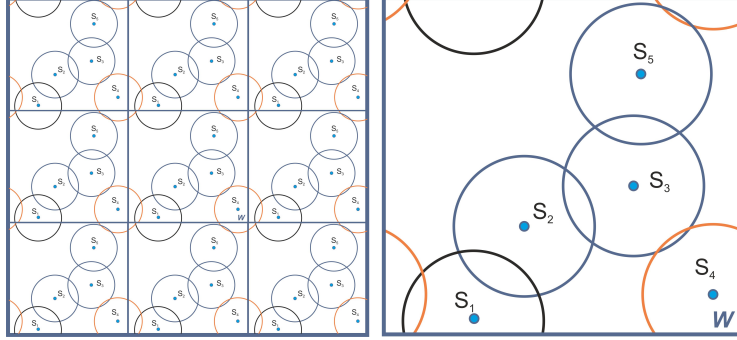


Fig. 1. Sketch of periodicity of RVEs generated by the PSMM: Left: Periodic extension of sphere system in Euclidean plane. Right: The midpoints of spheres $\{S_1, \dots, S_5\}$ are located in W and periodic boundary conditions are applied to the sphere system. The spheres with midpoints S_1 and S_4 represented in black and orange, respectively, overlap with the boundary of W . Thus, for both spheres, the parts that stick out of W at one side are included on the opposite side.

attraction of midpoints is applied alternately according to a modified version of the avoidance algorithm presented by Hirsch et al. (2015), which goes back to the force-biased algorithm introduced by Mosciński et al. (1989). For attraction of sphere midpoints a parametric random graph G is modeled such that midpoints connected by an edge in the graph are attracted to each other. A formal definition of the model graph G and a detailed description of the rearrangement algorithm is given in the Appendix.

Using the PSMM virtual RVEs in 2D and 3D with various constellations of porosity and average coordination number are generated, while the parameter ρ controlling pairwise overlap is fix with $\rho = 0.2$. Virtual RVEs generated by the PSMM are visualized in Figures 11, 12 and 13 for the 2D case and in Figure 8 for the 3D case. The influence of microstructure characteristics on mechanical properties for these virtual sphere systems is discussed in Section 3.

2.2. Assessment and homogenization of elastic properties

The microstructures generated by the PSMM described above have to be meshed appropriately such that they can be used as RVEs for finite element (FE) simulations. To accomplish this, the domain of the RVEs (Figure 2) is partitioned into 500×500 quadratic subdomains with an edge length of 8 nm. A careful mesh sensitivity analysis revealed that the maximum difference of the Young's modulus to simulations with a 1000×1000 mesh is below 10%, whereas coarsening the mesh to a 375×375 grid results in deviations of more than 25%. Then, a subdomain is considered as part of the ceramic phase if its center is located within a ceramic grain. Only in this case a finite element of the size of the subdomain is created, while otherwise the subdomain is considered as part of a pore and no element is created. This procedure results in a regular mesh of the considered RVE (Figure 2 (c)). Note that this results in a quasi-2D mesh, where the extension of the model

in z -direction is only one element wide and thus small compared to the x - and y -dimension of the model. Throughout the present paper isotropic linear elastic material behavior is assumed for the ceramic phase. The Young's modulus of the dense ceramic phase amounts to $E_0 = 360$ GPa and the Poisson ratio is $\nu = 0.3$. To assess the elastic stiffness tensor of the RVE small strains of $\epsilon = 0.1\%$ are applied to the box and the resulting global stresses are calculated by assuming periodic boundary conditions as described below. The FE calculations have been performed using the commercial software product Abaqus (ABAQUS, 2012) using hexagonal elements of type C3D8, with linear shape functions and full integration. This implies that the numerical solution of the problem is 3D in nature.

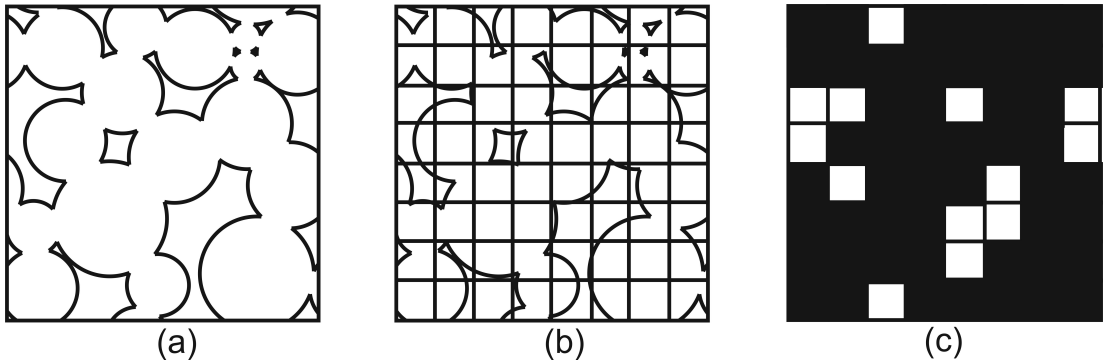


Fig. 2. Schematic of the meshing of a RVE, demonstrated on a slice through a 3D RVE: (a) structure with overlapping spheres generated by the stochastic model; (b) partitioning of the sampling window into subdomains; (c) creation of finite elements representing the ceramic phase. Note that the quasi-2D RVEs are discretized into 500×500 elements, to provide a reasonable resolution of the microstructures.

The use of RVEs in material simulations usually yields best results if periodic boundary conditions (PBCs) are applied, because free boundary conditions tend to cause a too compliant response, whereas fixed boundary conditions oftentimes result in a too stiff response. The concept is based on the work by Smit et al. (1998), covering the pure 2D case. The basis is that two opposite boundaries must be compatible in their deformation such that they always possess the same shape while the stresses are of opposite sign. Thus the displacement field is periodic leading to a continuous stress field over the RVE boundaries, see Smit et al. (1998). To satisfy these conditions, the degrees of freedom of equivalent nodes on opposite boundaries have to be coupled. This is done by equating the displacements of such nodes with the global strain, thus

$$u_x^R - u_x^L = \varepsilon_{xx} \cdot l_x \quad (2)$$

for the x -direction and

$$u_y^T - u_y^B = \varepsilon_{yy} \cdot l_y \quad (3)$$

for the y -direction, where u_x^R is the x -displacement of the right-hand-side node, u_x^L the x -displacement of the left-hand-side node, u_y^B the y -displacement of the bottom node and u_y^T the y -displacement of the top node. The global elastic strain tensor is denoted by ε and l_x and l_y are the extensions of the simulation domain in the respective directions. To achieve a full periodicity of the RVE, these relations have to be valid for every pair of nodes on opposite boundaries. To extend the concept of PBCs into the third dimension, it is necessary to formulate an equivalent relation for the degrees of freedom in the z -direction of the boundaries nodes, i.e.

$$u_z^F - u_z^R = \varepsilon_{zz} \cdot l_z \quad (4)$$

where u_z^F is the z -displacement of the front node and u_z^R the z -displacement of the rear node. In this way, both the quasi-2D as well as the 3D structures are fully periodic in all three Cartesian dimensions.

By applying such PBCs to the RVE it becomes possible to calculate the average Cauchy stress tensor $\bar{\sigma}_{RVE}$ as the volume integral over the local Cauchy stresses σ normalized by the total volume of the RVE in the current configuration V_{RVE} , such that

$$\bar{\sigma}_{RVE} = \frac{1}{V_{RVE}} \int_{p \in V_{RVE}} \sigma(p) dV \quad (5)$$

is obtained (Smit et al., 1998). For the quasi-2D case with an RVE of unit thickness, Equation (5) can be rewritten as

$$\bar{\sigma}_{RVE} = \frac{1}{V_{RVE}} \text{sym} \left[(\mathbf{x}^{V4} - \mathbf{x}^{V1}) \otimes \mathbf{f}^{V4} + (\mathbf{x}^{V2} - \mathbf{x}^{V1}) \otimes \mathbf{f}^{V2} \right] \quad (6)$$

where \mathbf{x} is the position vectors of the node given in the superscript and \mathbf{f} is the force vector of the corresponding corner node. The function $\text{sym}(\mathbf{A}) = 1/2 (\mathbf{A} + \mathbf{A}^T)$ represents the symmetric part of a second-order tensor \mathbf{A} , and the symbol \otimes represents the dyadic tensor product of two vectors as $\mathbf{A} = \mathbf{a} \otimes \mathbf{b}$ or $A_{ij} = a_i b_j$, in index notation. See Figure 3 for the definitions of the corner nodes.

In Figure 3 a three dimensional cell is shown, where the front face with nodes $V1 - V4$ corresponds to the definition in Equation (6). Dependent and independent nodes are highlighted by different greyscales. Boundary conditions are only applied on the independent nodes. With these definitions, Equation (6) can be extended to the 3D case in the following way:

$$\bar{\sigma}_{RVE} = \frac{1}{V_{RVE}} \text{sym} \left[(\mathbf{x}^{V4} - \mathbf{x}^{V1}) \otimes \mathbf{f}^{V4} + (\mathbf{x}^{V2} - \mathbf{x}^{V1}) \otimes \mathbf{f}^{V2} + (\mathbf{x}^{H1} - \mathbf{x}^{V1}) \otimes \mathbf{f}^{H1} \right]. \quad (7)$$

Using this approach it is possible to homogenize the 4-rank elastic stiffness tensor \mathbf{C} , defined by Hooke's law $\sigma = \mathbf{C} \varepsilon$. The RVE does not obey any particular symmetry relation, such that the stiffness tensor has 21 independent components, cf. Figure 4 where the stiffness tensor is represented in the Voigt notation. These independent components are calculated by applying six different load cases to the RVE in such

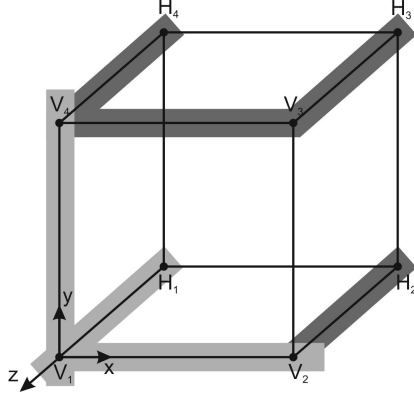


Fig. 3. Periodic cell with corner node definitions; independent nodes are marked in light grey, whereas dependent nodes are marked in dark grey.

a way that five of the six independent components of the strain tensor are zero. Hence uniaxial tensile strain in x , y and z -directions as well as pure shear strain in xy , yz and xz -shearing directions is applied, see Figure 4. With each load case it is possible to determine one column of the Voigt stiffness matrix that can then be transformed in the 4-rank stiffness tensor. Note that the Voigt stiffness matrix must be symmetric, which is however not enforced by our method, such that the validity of this condition provides a measure for the accuracy of the numerical procedure.

$$\mathbf{C} = \begin{pmatrix}
 C_{11} & C_{12} & C_{13} & C_{14} & C_{15} & C_{16} \\
 C_{21} & C_{22} & C_{23} & C_{24} & C_{25} & C_{26} \\
 C_{31} & C_{32} & C_{33} & C_{34} & C_{35} & C_{36} \\
 C_{41} & C_{42} & C_{43} & C_{44} & C_{45} & C_{46} \\
 C_{51} & C_{52} & C_{53} & C_{54} & C_{55} & C_{56} \\
 C_{61} & C_{62} & C_{63} & C_{64} & C_{65} & C_{66}
 \end{pmatrix}$$

Fig. 4. Six different load cases which are used to determine the elastic stiffness matrix given in the Voigt notation here. Note that the stiffness tensor is symmetric.

Using the relation

$$E = \frac{1}{S_{1111}}. \quad (8)$$

between the Young's modulus E and the compliance tensor $\mathbf{S} = \mathbf{C}^{-1}$, it is possible to calculate the Young's modulus of the quasi-2D RVE. Due to the finite size of the RVE, this procedure might result in a Young's modulus that is anisotropic, i.e. that depends on the choice of the loading direction. To remove this anisotropy, the Young's modulus of the quasi-2D RVE is calculated by rotating the stiffness

tensor with a step size of 1 degree before Equation (8) is applied and averaging over all resulting values is performed. This average value of E represents the Young's modulus of a quasi-isotropic material. Equation (8) can also be used for 3D RVEs. Using the described rotation with respect to all three axes within the 3D space, can lead to the problem, that not every possible combination of angles might be covered. In order to avoid this, an integral method, utilizing the Haar measure as shown in Hackl (1999), is applied to calculate an isotropic mean stiffness tensor and subsequent calculate the Young's modulus and the Poisson's ratio.

3. Results and Discussion

In this section, the influence of microstructural parameters, such as porosity f_p and the average coordination number \tilde{N}_C , on mechanical properties of porous structures is evaluated. This is accomplished by calculating the normalized Young's modulus E/E_0 of each structure and comparing it to both microstructural parameters. We start with introducing the average coordination number as microstructural parameter. The importance of this parameter is best motivated on quasi-2D microstructures, where it is shown that the mechanical properties depend on this parameter in a unique way. After that it is demonstrated that the average coordination number describes the properties of fully 3D RVEs in the same way as that of 2D structures. Finally, the physical importance of this parameter is demonstrated by closely analyzing the load transfer paths through the porous structures.

3.1. Average coordination number

To motivate the introduction of the average coordination number as further microstructural parameter to describe mechanical properties of porous structures, we start by analyzing the dependence of the elastic properties on the porosity of quasi-2D microstructures. In Figure 5 it is shown that E/E_0 exhibits a generally decreasing trend for increasing porosity f_p , which is in good qualitative agreement with findings for porous ceramics (Smolin et al., 2014; Yoshimura et al., 2007), while a similar trend can be observed for other mechanical properties, as the bulk modulus (Munro, 2001). However, over the complete range of f_p a strong scattering of the values of E/E_0 for a constant porosity is observed for the quasi-2D models. This indicates that at least in 2D there must be further microstructural parameters besides the porosity that possess a very pronounced influence on the stiffness of the porous material.

In a first step to introduce such a new microstructural parameter, the values of \tilde{N}_C obtained for the different microstructures investigated here are sub-divided into three categories as indicated in Figure 5. The subdivision is done according to a normalization of \tilde{N}_C with respect to its highest (\tilde{N}_C^{\max}) and lowest (\tilde{N}_C^{\min}) value

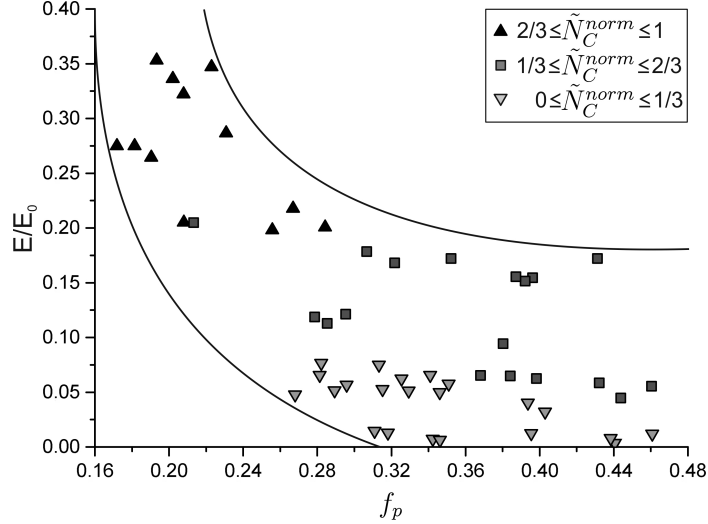


Fig. 5. Normalized Young's modulus E/E_0 of all generated RVEs plotted over their porosity f_p . The different symbols represent different classes of the normalized average coordination number $\tilde{N}_C^{\text{norm}}$, as given in the legend and defined in the text. The solid lines are mere visual aids to indicate the upper and lower limits of the values obtained.

appearing in the investigated microstructures, as

$$\tilde{N}_C^{\text{norm}} = \frac{\tilde{N}_C - \tilde{N}_C^{\text{min}}}{\tilde{N}_C^{\text{max}} - \tilde{N}_C^{\text{min}}}. \quad (9)$$

It can be seen that E/E_0 separates into three distinct regions that can be correlated with the three classes of $\tilde{N}_C^{\text{norm}}$. The highest class $2/3 \leq \tilde{N}_C^{\text{norm}} \leq 1$ can be directly linked to $E/E_0 \geq 0.2$ (except for one value). This separation can be also observed for $1/3 \leq \tilde{N}_C^{\text{norm}} \leq 2/3$ and $0 \leq \tilde{N}_C^{\text{norm}} \leq 1/3$. The different classes can be related to the values in the middle and to the lowest values of E/E_0 , respectively.

The correlation between \tilde{N}_C and f_p is visualized in Figure 6, where a general decrease of \tilde{N}_C with increasing f_p is seen. This is in agreement with findings reported in the literature that there is in fact some correlation between \tilde{N}_C and f_p , see e.g. (German, 2014; Arzt, 1982; Luding et al., 2005; Liu et al., 2010). The average coordination number \tilde{N}_C increases during densification of a porous microstructure, which agrees with the data provided in Figure 6. However, it has also been found that there is a strong scattering, in particular for values $f_p \geq 0.25$, such that the correlation merely reflects a trend in the values, but no strict functional dependence. The observations that (i) porosity does not uniquely characterize elastic properties of porous materials, see also Cyterman (1987), and that (ii) different classes of correlation numbers \tilde{N}_C correspond to different classes of stiffness provide a first motivation for the hypothesis that the stiffness should be strongly correlated with the average coordination number. Hence, the average coordination number, which is known in relation to aggregates, see Jefferson (2002), is proposed here as a new

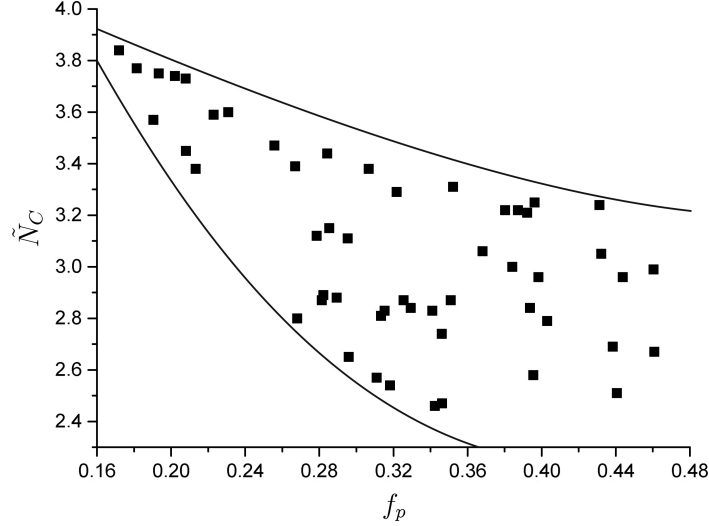


Fig. 6. Plot of the average coordination number \tilde{N}_C versus porosity f_p . The solid lines are mere visual aids to indicate the upper and lower limits of the values obtained.

microstructural parameter in terms of the description of the elastic properties of solid porous materials. This parameter is a measure for the average number of sintered, i.e. in the present paper overlapping, neighboring grains (German, 2014) and it appears to be natural to assume that a higher amount of overlaps will lead to better load transmission within the structure and thus to a higher stiffness.

3.2. Influence of the average coordination number on elastic properties

In the following the influence of the average coordination number \tilde{N}_C on the elastic properties of the porous microstructure is assessed further to verify whether it can account for the scattering of E/E_0 at constant porosities. To accomplish this, the normalized stiffnesses of the porous microstructures are plotted against their average coordination numbers in Figure 7. It is seen immediately that there exists a much closer correlation between stiffness and coordination number than between stiffness and porosity. In fact, there is only a rather small scattering of the stiffness for given coordination numbers, where it is found that higher porosities lead to slightly more compliant material behavior. The quantitative relationship between E/E_0 and \tilde{N}_C is visualized as a fit line in Figure 7. The quadratic fit function follows the relation

$$\frac{E}{E_0} = m_1 \tilde{N}_C + m_2 \tilde{N}_C^2 + b, \quad (10)$$

where m_1 , m_2 and b are the linear and quadratic prefactors and the axis offset, respectively. The estimated fit parameters are listed in Table 1. For small values of \tilde{N}_C non-linear effects occur, which arise due to the enforced global connectivity

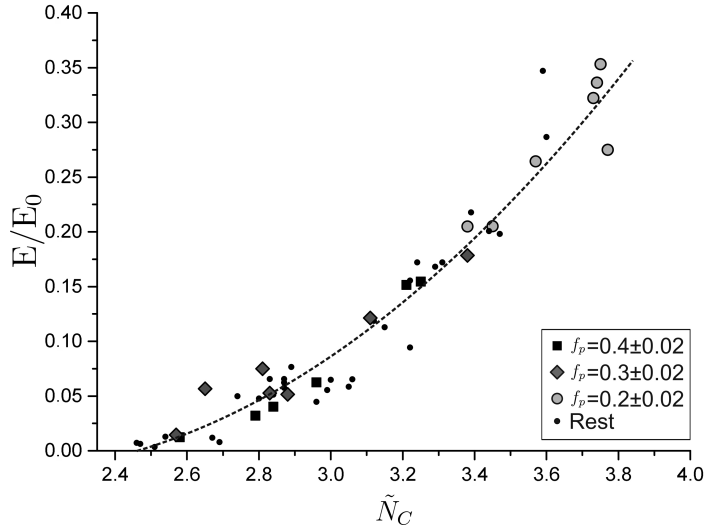


Fig. 7. Normalized Young's modulus E/E_0 of porous microstructures plotted over their average coordination number \tilde{N}_C . Data is subdivided into the three classes of porosities (f_p) provided in the legend. All other data points (indicated as 'Rest') do not belong to a specific porosity class. The dashed line represents the quadratic fit to the data points as described in the text.

of the microstructures, giving a bias towards the selection of microstructures with higher stiffnesses at high porosities. Considering RVEs with porosities in the ranges 0.18 - 0.22, 0.28 - 0.32 and 0.38 - 0.42 separately, it is observed that microstructures with the lowest porosities exhibit the highest values for E/E_0 and \tilde{N}_C , whereas structures with higher porosities possess less stiffness, see Figure 7. Thus, it can be said that for the 2D models, the average coordination number is the most fundamental parameter to describe their elastic properties, whereas the porosity is a correction on top of that parameter.

Table 1: Estimated parameters of the quadratic regression model given in Equation (10) and visualized in Figures 7 and 10.

Figure	m_1	m_2	b
7	-0.482	0.119	0.482
10	-0.367	0.037	1.088

The fit of the quadratic model shows that there is a very strong correlation between \tilde{N}_C and E/E_0 , in contrast to the much larger scattering occurring when E/E_0 is related to f_p . The relation between the average coordination number and the stiffness of a microstructure is almost unique, because the porosity f_p influences

the stiffness E/E_0 at constant values of the average coordination number \tilde{N}_C only slightly. In summary we find that our results are consistent with the hypothesis that the average coordination number is the main microstructural parameter influencing the stiffness of a porous sinter ceramic. We note here, that the presented quadratic relations are mere fit functions, whose purpose it is to clearly demonstrate the strong and unique correlation between elastic properties of a granular porous material and its average coordination number. It will be the scope of future work to develop a proper theoretical description of such a relationship.

3.3. Fully 3D representative volume elements

In the following the results for fully 3D RVEs are presented and discussed. One of the 3D RVEs is shown in Figure 8, where the microstructure and the maximum principle stresses for tensile loading along the three Cartesian axes are presented. In Figure 9, it can be seen that E/E_0 reaches to higher values in the 3D case.

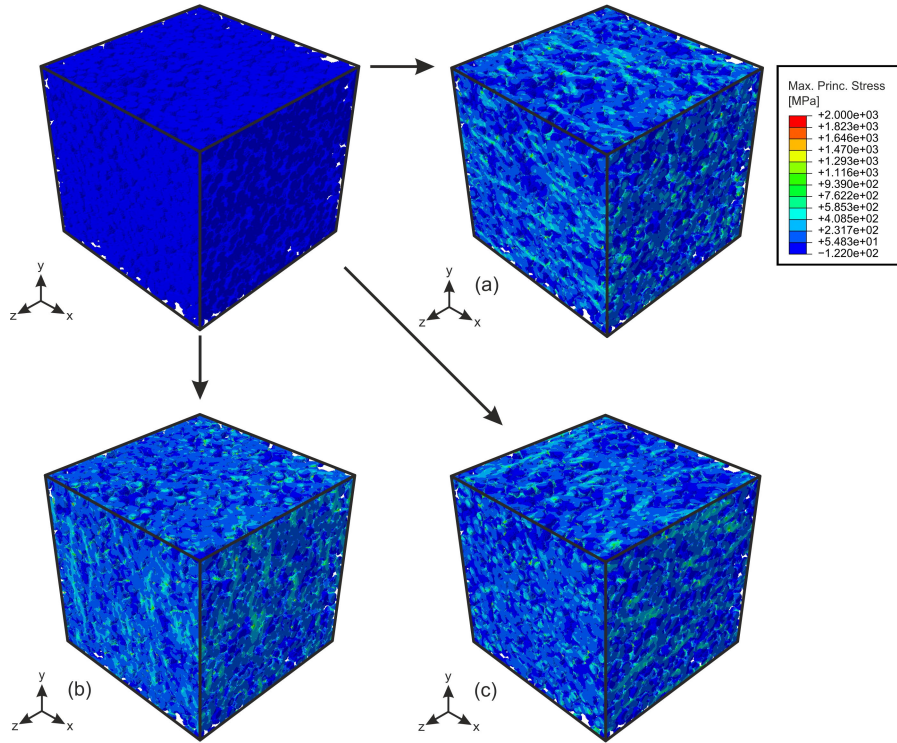


Fig. 8. Microstructure of one 3D RVE (top left) and maximum principle stresses for tensile loading along the x , y and z -axis in subfigures (a), (b), and (c), respectively.

Furthermore, in contrast to the 2D case, E/E_0 and f_p are strongly and also rather uniquely correlated. It will be shown later that this can be attributed to the limited

number of paths through which forces can be transferred through 2D structures, whereas in 3D there is always a plenty of load transfer paths. However, also in 3D the correlation between stiffness and average coordination number \tilde{N}_C is still strong as can be seen in Figure 10. Furthermore, also in the 3D case, a quadratic fit describes the results very well, see Table 2 for the fitted parameters.

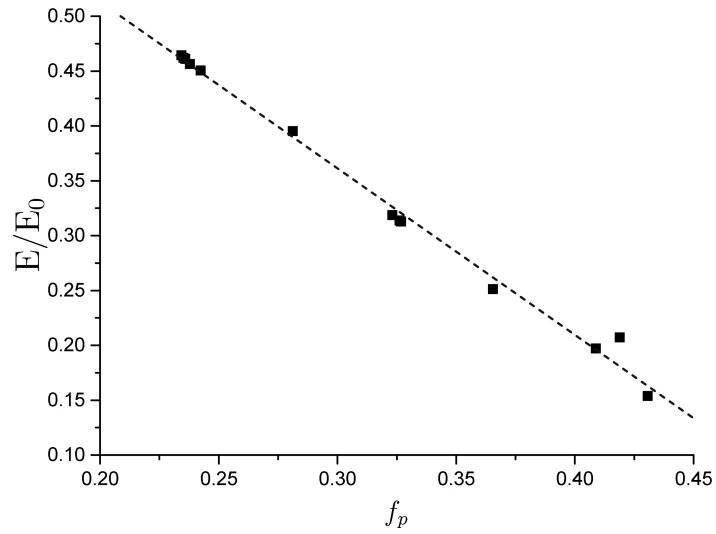


Fig. 9. Normalized Young's modulus E/E_0 of porous microstructures plotted over their porosity f_p . Note that the presented values have been computed for 3D RVEs.

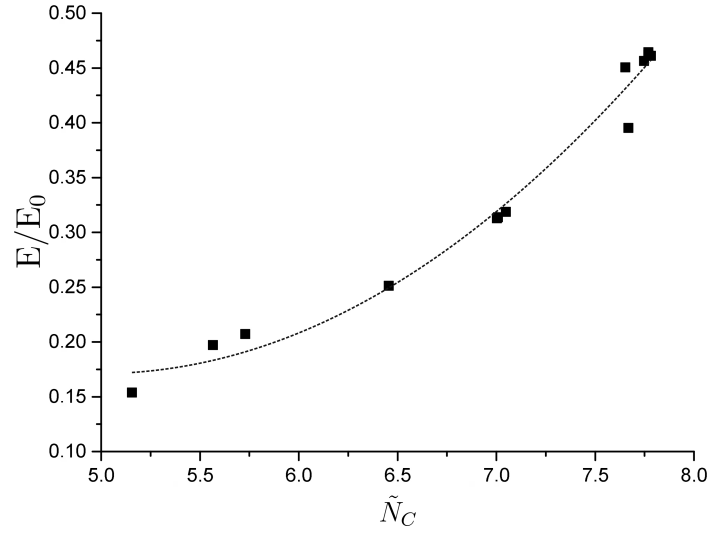


Fig. 10. Normalized Young's modulus E/E_0 of porous microstructures plotted over their average coordination number \tilde{N}_C . Note that the presented values have been computed for 3D RVEs.

From the comparison of 2D and 3D results it can be stated that the parameter of the average coordination number \tilde{N}_C describes both types of results with the same strong correlation and limits the scattering of data even for the 2D case, where there is no good correlation between the porosity and the stiffness of the material. Hence, it can be stated that \tilde{N}_C seems to be the more fundamental parameter to describe the mechanical properties of porous materials.

Table 2: \tilde{N}_C, f_p and E/E_0 of the structures shown in Figures 11 to 13. Note that E/E_0 refers to the homogenized value for E , as described above.

Figure	Structure	\tilde{N}_C	f_p	E/E_0
11	<i>A</i>	2.46	0.342	0.007
12	<i>B</i>	3.84	0.172	0.270
13	<i>C</i>	3.31	0.352	0.170

3.4. Load transfer paths

A further motivation for the introduction of the average coordination number as an essential microstructural parameter with an immediate physical meaning can be drawn from taking a closer look on the way the applied force is transmitted through the 2D porous microstructure. Figure 11 (structure *A*) shows the plot of the maximum principle stresses for a simulated microstructure after deformation to a tensile strain of 0.1% in x -direction. The microstructure has a porosity $f_p = 0.342$ and its average coordination number is $\tilde{N}_C = 2.46$, which is the lowest value of all RVEs considered in the present paper. It clearly exhibits well-defined load paths along which the forces are transmitted and which hence indicate the most favorable way for the load distribution within the microstructure. The highest stresses occur at the sinter necks, which represent the smallest cross-sectional area of two overlapping particles.

The porosity of structure *B* (Figure 12) is 0.172, which is about half the value of structure *A*. The average coordination number is the largest of all structures investigated here and amounts to $\tilde{N}_C = 3.84$, such that grains on average exhibit a higher number of overlaps. Thus, a larger number of force transmission paths through the material exists. Moreover, the overall stress level at the same tensile strain in structure *B* is higher than that in structure *A*, indicating that *B* is the stiffer structure. A quantitative comparison of the normalized Young's moduli between structure *A* and *B* reveals that they differ by a factor of approximately 38 (structure *A*: $E/E_0 = 0.007$, structure *B*: $E/E_0 = 0.27$; cf. Table 2. Furthermore, one salient feature of structure *B* is that there are regions in which the stresses are significantly smaller than in the rest of the material. These regions seem to be those

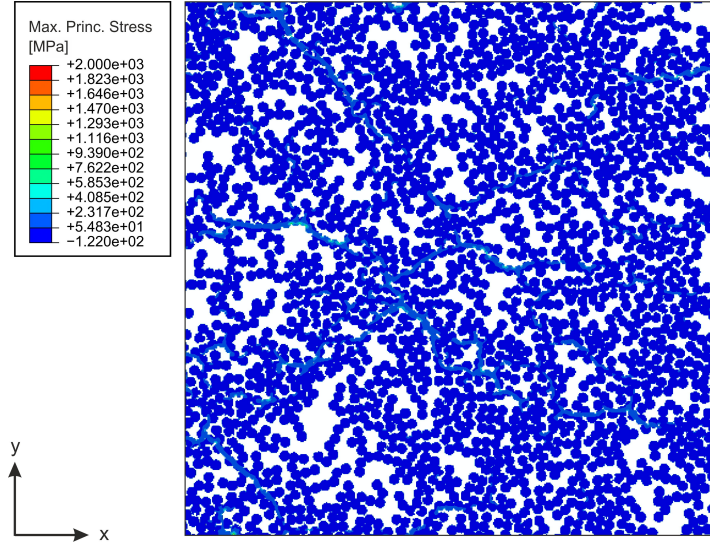


Fig. 11. Plot of the maximum principle stress for structure *A* (see text) with $\tilde{N}_C = 2.46$ and $f_p = 0.342$ at a tensile strain of $\epsilon_{xx} = 0.1\%$. The normalized Young's modulus amounts to $E/E_0 = 0.007$.

places where larger gaps occur and the connectivity of the microstructure is locally disturbed such that no force is transmitted through such regions.

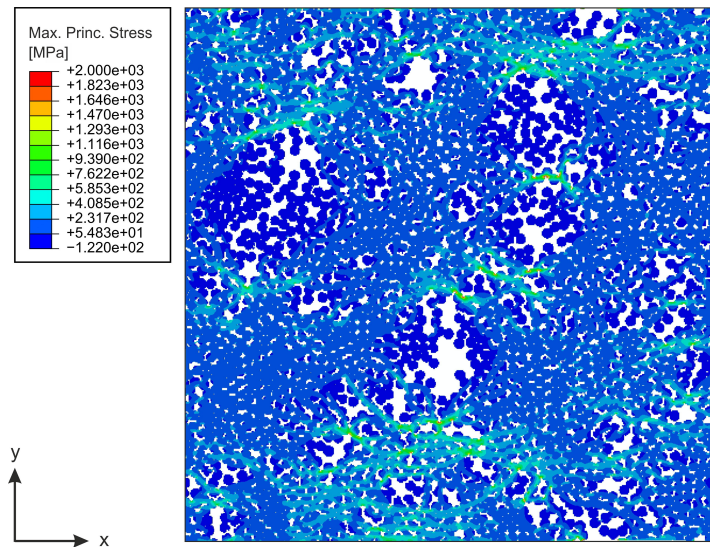


Fig. 12. Plot of the maximum principle stress for structure *B* with $\tilde{N}_C = 3.84$ and $f_p = 0.172$ at a tensile strain of $\epsilon_{xx} = 0.1\%$. The normalized Young's modulus E/E_0 is 0.27.

In Figure 13 (structure *C*), finally, the force transmission through a structure is

represented that is characterized by a rather high porosity of $f_p = 0.352$, which is slightly higher than that of structure *A*. However, the normalized Young's modulus of structure *C* is $E/E_0 = 0.17$ and thus more than a factor of 24 higher than that of structure *A*. This is attributed to the significantly better connectivity, expressed by the larger average coordination number of $\tilde{N}_C = 3.31$ in this structure. A better connectivity between the grains allows for a more efficient force transmission through the structure. The load paths in structure *C* show a horizontal pattern, which is also favored by the chain-like regular structure in which the grains are arranged, with only some agglomerations of grains. Note that – as throughout the present paper – the normalized Young's modulus E/E_0 of this structure is calculated as a homogenized value, as described in section 2.2.

Visual inspection of the stress distributions in the mechanically loaded microstructures thus confirms our previous observation that there is a strong correlation between the average coordination number and stiffness, whereas in the quasi-2D case the influence of porosity on stiffness is much weaker and shows a much larger scattering.

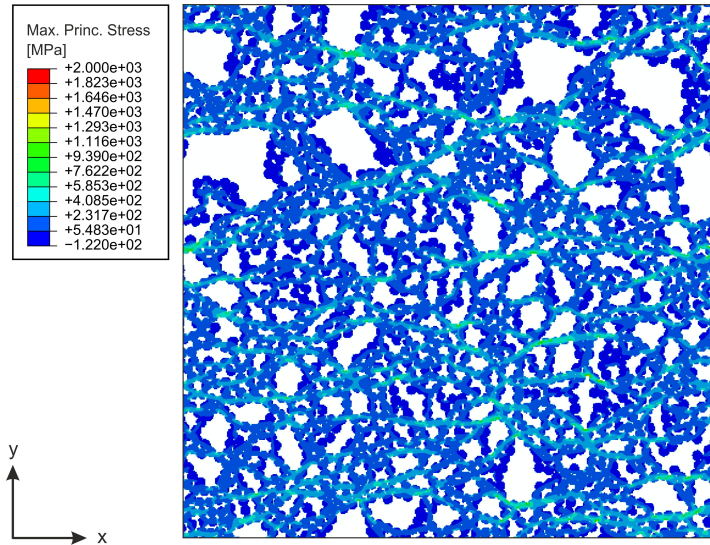


Fig. 13. Plot of the maximum principle stress for structure *C* with $\tilde{N}_C = 3.31$ and $f_p = 0.352$ at a tensile strain of $\epsilon_{xx} = 0.1\%$. The normalized Young's modulus E/E_0 is 0.17.

4. Conclusions

In this computational study the mechanical behavior of porous ceramics has been investigated. A wide range of RVEs has been generated by the aid of a parametric stochastic microstructure model (PSMM), which is based on methods from stochas-

tic geometry and graph theory. To mimic typical microstructures of sintered ceramics, the spheres representing ceramic particles are allowed to overlap, which essentially models the formation of sinter necks. To characterize the mechanical behavior of such RVEs, the finite element method has been applied to simulate the elastic response of different microstructures. By using homogenization methods it has been possible to calculate a representative stiffness tensor and hence the effective Young's modulus for each RVE.

The presented results show a decrease of Young's modulus of the porous structures with increasing porosity, which is in agreement with the findings from both experimental and computational studies. However, comparing the results of 2D and 3D models reveals a large scattering of Young's modulus for 2D RVEs with the same porosity, whereas for 3D models there is a strict correlation between porosity and stiffness of the material. This motivates the introduction of the average coordination number as a new microstructural parameter to describe the stiffness of porous ceramics. The average coordination number is a measure for the average number of sinter necks that each ceramic grain forms to its neighboring grains. Hence, it provides a measure for the connectivity within the porous network of grains, which in turn characterizes the efficiency of load transfer through the structure and thus its stiffness. This parameter has a clear physical interpretation and it can precisely describe the 2D results, where different structures with the same porosity can have very different elastic properties.

The combination of stochastic and mechanical modeling has revealed that the influence of this topological parameter on the resulting Young's modulus is more fundamental than the porosity. In fact, even for the 2D models it could be shown that for given values of the average coordination number a quite unique relation to the stiffness of the microstructure exists and that only a small spread in the resulting Young's modulus occurs, which can be attributed to variations in porosity. Hence, our main conclusion is that connectivity properties play an important role for mechanical behavior of sintered materials. In particular, the average coordination number should be considered as a fundamental parameter to characterize the mechanical behavior of sintered porous ceramics, which is, however, difficult to assess by experimental methods.

Acknowledgements

The authors would like to acknowledge co-funding of the project CeraMer by the European Union within the Ziel2 program and the state Northrhine-Westphalia through NRW.Bank under grant number 30 01 637 02.

Appendix

In the following, we give formal definitions of the model graph G and the rearrangement algorithm of the sphere system which is used for the generation of virtual RVEs

described in Section 2.1. The model graph G consists of the edges of the minimum spanning tree (Thulasiraman and Swamy, 1992) on $\{S_i\}_{i=1}^n$ with respect to the distance δ , introduced in Section 2. The minimum spanning tree is a connected graph on $\{S_i\}_{i=1}^n$ such that the total edge length is minimized. In a further step we add edges to the graph according to the following parametric model. At first, we attach random marks $\{M_i\}_{i=1}^n$ to the midpoints of spheres. These marks are independent and identically distributed such that $\mathbb{P}(M_1 = j) = \theta_j$ for each $j \in \{1, \dots, 5\}$ with model parameters $\theta_1, \dots, \theta_5 \in [0, 1]$ where $\theta_1 + \dots + \theta_5 = 1$. Note that these marks are never changed during the rearrangement of sphere midpoints. We connect each midpoint S_i to its M_i nearest neighbors by edges in the graph, where the nearest neighbors are computed with respect to δ . The model graph with parameter vector $\boldsymbol{\theta} = (\theta_1, \dots, \theta_5)$ is denoted by $G_{\boldsymbol{\theta}}$. For simulation purposes we choose $\theta_4 = \theta_5 = 0$ in dimension $d = 2$, since there is less space available around a single sphere in 2D compared to 3D.

The rearrangement of the sphere system consists of iterative repulsion and attraction steps. At first the repulsion step is described. Let $\{S_i\}_{i=1}^n$ be the system of midpoints of spheres with constant radius $r > 0$ and $0 < F_{\min} < F_{\max}$ be positive numbers. In each step of the force-biased algorithm, every midpoint is translated by a vector, the Euclidean norm of which is bounded from below by F_{\min} and bounded from above by F_{\max} . In the case of repulsion we define for each $i \in \{1, \dots, n\}$ the vector

$$v_i = \frac{1}{2} \sum_{j=1, j \neq i}^n c_{i,j} (S_i -_w S_j) \mathbb{1}\{O_{i,j} \geq \alpha\}, \quad (11)$$

where for each $i, j \in \{1, \dots, n\}$ we put

$$c_{i,j} = r(2 - \alpha) - \delta(S_i, S_j) \quad (12)$$

for some parameter $\alpha < 1$. The symbol $-_w$ denotes subtraction with respect to periodic boundary conditions in the observation window W . After scaling the vector v_i such that $F_{\min} \leq \|v_i\| \leq F_{\max}$, it is the displacement vector for the i -th sphere midpoint in one iteration during the repulsion process. For each $j_0 \in \{1, \dots, n\} \setminus \{i\}$ the vector $S_i -_w S_{j_0}$ in the sum of v_i is weighted by the length of the line segment between S_i and S_{j_0} which is covered by the spheres centered in S_i and S_{j_0} , where the radii are scaled by $1 - \alpha/2$. The reason for scaling the radii by $1 - \alpha/2$ is the following. If all summands of v_i are zero except for the one corresponding to the j_0 -th sphere, the definition of c_{i,j_0} leads to $O_{i,j_0} = \alpha$ after one repulsion step. A scaling of radii for computing the displacement vector is also applied in the classical force-biased algorithm, see Mosciński et al. (1989). After the repulsion step, the new system of sphere midpoints is given by $\{S_i^{(\text{rep})}\}_{i=1}^n$, where

$$S_i^{(\text{rep})} = S_i + \frac{v_i}{\|v_i\|} \max\{F_{\min}, \min\{F_{\max}, \|v_i\|\}\}, \quad (13)$$

for each $i \in \{1, \dots, n\}$. We set $\{S_i\}_{i=1}^n = \{S_i^{(\text{rep})}\}_{i=1}^n$ and repeat this procedure

until $\sum_{i=1}^n \|v_i\| < 0.01$ or 1000 iterations are done. Note that in general the force-biased algorithm would not stop after 1000 iterations, but in this case we apply the force-biased algorithm several times to the system of sphere midpoints.

The algorithm for attraction of sphere midpoints is similar to the one for repulsion. For a given sphere system with midpoints $\{S_i\}_{i=1}^n$, with constant radius $r > 0$ and marks $\{M_i\}_{i=1}^n$, we compute the graph $G = G_{\theta}$ for a given parameter vector θ . The edge set of G is denoted by E . Similar to the repulsion step, for each $i \in \{1, \dots, n\}$ we define a vector

$$u_i = \frac{1}{2} \sum_{(S_i, S_j) \in E} c_{i,j} (S_i -_w S_j) \mathbf{1}\{O_{i,j} < \alpha\}, \quad (14)$$

with coefficients $c_{i,j}$ from Equation (12). For each $j_0 \in \{1, \dots, n\} \setminus \{i\}$ the following holds. If all summands of v_i are zero except for the one corresponding to the j_0 -th sphere, the definition of c_{i,j_0} leads to $O_{i,j_0} = \alpha$ if $(S_i, S_{j_0}) \in E$ after application of one attraction step. The sphere system $\{S_i^{(\text{att})}\}_{i=1}^n$ after one attraction step is given by

$$S_i^{(\text{att})} = S_i + \frac{u_i}{\|u_i\|} \max\{F_{\min}, \min\{F_{\max}, \|u_i\|\}\}, \quad (15)$$

for each $i \in \{1, \dots, n\}$. Attraction of the sphere system is iterated in the same way as repulsion of the sphere system, i.e. until $\sum_{i=1}^n \|u_i\| < 0.01$ or 1000 iterations are done.

In the rearrangement of sphere midpoints the initial sphere system plays an important role. Since we want to have a homogeneous sphere system we chose α in the first repulsion step as

$$\alpha = 1 - \frac{1}{r} \sqrt[d]{\frac{0.6\nu_d(W)}{\kappa_d n}}, \quad (16)$$

where κ_d denotes the volume of the d -dimensional unit sphere. With this choice of α the volume fraction of a non-overlapping sphere system with constant radius $r(1 - \alpha)$ is 0.6. The value 0.6 is chosen since the classical force-biased algorithm, which is similar to our repulsion algorithm, is able to generate packings of non-overlapping spheres with volume fraction higher than 0.6 (Mosćiński et al., 1989). Thus, after applying the repulsion algorithm the first time we get a sphere system with non-overlapping spheres corresponding to the constant radius $r(1 - \alpha)$. Note that $\alpha < 0$ if the volume fraction for the non-overlapping sphere system is smaller than 0.6. The first repulsion step leads to a more regular point pattern of sphere midpoints. In all further repulsion and attraction steps during the rearrangement of sphere midpoints, α is given by the model parameter $\rho \in [0, 1]$, which controls overlapping between the spheres. Furthermore, we let $F_{\min} = 1, F_{\max} = 20$ fixed during the rearrangement procedure.

References

- ABAQUS (2012). Abaqus version 6.12, *Dassault Systems*.
- Arzt, E. (1982). The influence of an increasing particle coordination on the densification of spherical powders, *Acta Metallurgica* **30**: 1883–1890.
- Asmani, M., Kermal, C., Leriche, A. and Ourak, M. (2001). Influence of porosity on Young’s modulus and Poisson’s ratio in alumina ceramics, *Journal of the European Ceramic Society* **21**: 1081–1086.
- Chiu, S. N., Stoyan, D., Kendall, W. S. and Mecke, J. (2013). *Stochastic Geometry and its Applications*, 3rd edn, J. Wiley & Sons, Chichester.
- Cyterman, R. (1987). A new way to investigate the dependance of elastic moduli on the microstructure of porous materials, *Powder Metallurgy International* **19**(4): 27–30.
- Diebels, S. and Steeb, H. (2002). The size effect in foams and its theoretical and numerical investigation, *Proc. R. Soc. Lond. A* **458**: 2869–2883.
- Gatt, J.-M., Monerie, Y., Laux, D. and Baron, D. (2005). Elastic behavior of porous ceramics: Application to nuclear fuel materials, *Journal of Nuclear Materials* **336**: 145–155.
- German, R. (2014). Coordination number changes during powder densification, *Powder Technology* **256**: 368–376.
- Göring, J., Hackemann, S. and Kanka, B. (2007). WHIPOX®: Ein faserverstärkter oxidkeramischer Werkstoff für Hochtemperatur-Langzeitanwendungen, *Materialwissenschaft und Werkstofftechnik* **38**(9): 766–772.
- Hackl, K. (1999). On the representation of anisotropic elastic materials by symmetric irreducible tensors, *Continuum Mech. Thermodyn.* **11**: 353–369.
- Hirsch, C., Gaiselmann, G. and Schmidt, V. (2015). Asymptotic properties of collective re-arrangement algorithms, *European Series in Applied and Industrial Mathematics: Probability and Statistics* **9**: 236–250.
- Jauffres, D., Liu, X. and Martin, C. (2011). Fracture mechanics of porous ceramics using discrete element simulations, *Procedia Engineering* **10**: 2719–2724.
- Jefferson, G. (2002). The elastic response of a cohesive aggregate - a discrete element model with coupled particle interaction, *Journal of the Mechanics and Physics of Solids* **50**: 2539–2575.
- Liu, X., Martin, C., Delette, G. and Bouvard, D. (2010). Elasticity and strength of partially sintered ceramics, *Journal of the Mechanics and Physics of Solids* **58**: 829–842.
- Luding, S., Manetsberger, K. and Müller, J. (2005). A discrete model for long time sintering, *Journal of the Mechanics and Physics of Solids* **53**: 455–491.
- Magdeski, J. (2010). The porosity dependence of mechanical properties of sintered alumina, *Journal of the University of Chemical Technology and Metallurgy* **45**(2): 143–148.
- Mattoni, M., Yang, J., Levi, C. and Zok, F. (2001). Effects of matrix porosity on the mechanical properties of a porous-matrix, all-oxide ceramic composite, *Journal*

- of the *American Ceramic Society* **84**(11): 2594–2602.
- Mosciński, J., Bargie, M., Rycerz, Z. and Jakobs, P. (1989). The force-biased algorithm for the irregular close packing of equal hard spheres, *Molecular Simulation* **3**: 201–212.
- Munro, R. (2001). Effective medium theory of the porosity dependence of bulk modulus, *Journal of the American Ceramic Society* **84**(5): 1190–1192.
- Nanjangud, S., Brezny, R. and Green, D. (1995). Strength and Young's modulus behaviour of a partially sintered porous alumina, *Journal of the American Ceramic Society* **73**(1): 266–268.
- Rice, R. (1984). Pores as fracture origins in ceramics, *Journal of Materials Science* **19**: 985–914.
- Roberts, A. and Garboczi, E. (2000). Elastic properties of model porous ceramics, *Journal of the American Ceramic Society* **83**(12): 3041–3048.
- Roschning, B. and Huber, N. (2016). Scaling laws of nanoporous gold under uniaxial compression: Effects of structural disorder on the solid fraction, elastic poisson's ratio, young's modulus and yield strength, *Journal of the Mechanics and Physics of Solids* **92**: 55–71.
- Sadowski, T. and Samborski, S. (2003). Modeling of porous ceramics response to compressive loading, *Journal of the American Ceramic Society* **86**(12): 2218–2221.
- Schmücker, M., Grafmüller, A. and Schneider, H. (2003). Mesostructure of WHIPOX all oxide CMCs, *Composites: Part A* **34**(7): 613–622.
- Smit, R., Brekelmans, W. and Meijer, H. (1998). Prediction of the mechanical behaviour of nonlinear heterogeneous systems by multi-level finite element modeling, *Computer Methods in Applied Mechanics and Engineering* **155**: 181–192.
- Smolin, A., Roman, N., Konovalenk, I., Eremina, G., Buyakova, S. and Psakhie, S. (2014). 3D simulation of dependence of mechanical properties of porous ceramics on porosity, *Engineering Fracture Mechanics* **130**: 53–64.
- Thulasiraman, K. and Swamy, M. N. S. (1992). *Graphs: Theory and Algorithms*, J. Wiley & Sons, New York.
- Wagh, A., Singh, J. and Poeppl, R. (1993). Dependence of ceramic fracture properties on porosity, *Journal of Materials Science* **28**: 3589–3593.
- Wiederhorn, S. (1984). Brittle fracture and toughening mechanisms in ceramics, *Annual Review of Materials Science* **14**: 373–403.
- Yoshimura, H., Molisani, A., Narita, N., Cesar, P. and Goldenstein, H. (2007). Porosity dependence of elastic constants in aluminum nitride ceramics, *Materials Research* **10**(2): 127–133.
- Zok, F. and Levi, C. (2001). Mechanical properties of porous-matrix ceramic composites, *Advanced Engineering Materials* **3**(1-2): 15–23.